

Article

Axial Compression Test and Numerical Investigation of Concrete-Filled Double-Skin Elliptical Tubular Short Columns

Jingzhe Li ¹, Qihan Shen ^{1,*}, Jingfeng Wang ¹, Beibei Li ¹ and Guoqiang Li ²¹ College of Civil Engineering, Hefei University of Technology, Hefei 230009, China² Anhui Key Laboratory of Civil Engineering Structures and Materials, Hefei University of Technology, Hefei 230009, China

* Correspondence: qihanshen667@hfut.edu.cn

Abstract: To probe into the performance of concrete-filled double-skin elliptical steel tubular (CFDEST) members, this paper designs and conducts an experiment on CFDEST short columns imposed with axial pressure, and finite element (FE) models of the axially compressed CFDEST stub columns are established and verified by the test outcomes, taking the influences of elliptical cross-section and hollow ratio into account. The impressions of various parameters, such as hollow ratio, diameter-to-thickness ratio, aspect ratio and so on, on the load-bearing capacity, initial rigidity and ductility property were investigated systematically. Moreover, the typical failure modes, contact pressure and concrete longitudinal stress of the axially compressed CFDEST short column are revealed. In light of the findings acquired by the laboratory tests and numerical analyses, the calculation formulae for evaluating the axial compress capacity of the CFDEST short column are proposed by taking the impact of the sectional aspect ratio and hollow ratio into account. The results indicate that the failure morphologies of axially compressed CFDEST short columns mainly include outward local bulges of the outside EST, the inward bulges of the inside EST and the crushing of core concrete. The axial compress capacity of the CFDEST short column would increase with the decrease in the sectional hollow ratio and aspect ratio. The calculation method is proved to be an accurate and reliable approach to evaluate the axial compress capacity of the CFDEST short column.

Keywords: concrete-filled double-skin elliptical steel tube; axial compression test; numerical analysis; failure mode; design method



Citation: Li, J.; Shen, Q.; Wang, J.; Li, B.; Li, G. Axial Compression Test and Numerical Investigation of Concrete-Filled Double-Skin Elliptical Tubular Short Columns. *Buildings* **2022**, *12*, 2120. <https://doi.org/10.3390/buildings12122120>

Academic Editor: Jan Fort

Received: 31 October 2022

Accepted: 15 November 2022

Published: 2 December 2022

Publisher's Note: MDPI stays neutral with regard to jurisdictional claims in published maps and institutional affiliations.



Copyright: © 2022 by the authors. Licensee MDPI, Basel, Switzerland. This article is an open access article distributed under the terms and conditions of the Creative Commons Attribution (CC BY) license (<https://creativecommons.org/licenses/by/4.0/>).

1. Introduction

A concrete-filled steel tube (CFST) was first developed and applied in practical engineering structures in the early 20th century and it was favoured and considered by many scholars and engineers, thanks to its excellent mechanical properties and economic benefits compared to reinforced concrete members [1–3]. During the last several decades, hundreds of studies on the loading mechanism and design methods of CFST members, joints, frames and structures under static (i.e., compression [4], bending [5], shear [6] and torsion [7]), dynamic (seismic [8,9], impact [10] and explosion [11]) and extreme loads [12,13] have been systematically presented. In line with the above research, the basic theories, such as the simple superposition principle [14], the unified strength rule [15] and so on, have been developed and design specifications of CFST structures in various regions (i.e., AISI 360-05 [16], EC 4 [14], GB 50396-2014 [17]) have been set.

On this basis, in order to further reduce the volume weight of the CFST structures and improve their loading behaviours, the concrete-filled double-skin steel tube (CFDST), one kind of composite member composed of infilled core concrete, and inside and outside steel hollow sections in a concentric arrangement, is developed. Compared to normal CFST members, a CFDST member has the characteristics of lighter weight, higher strength and larger bending stiffness [18–21]. Due to these superiorities, the CFDST members have been

gradually popularized in wind-power towers, high-rise buildings and transmission tower structures, which offers a good application prospect in civil engineering [22,23]. Under the background of research requirements for CFST structures in engineering practice, a collection of investigations on the mechanical properties of CFST members with common sections (i.e., square and circular sections) was launched by a number of scholars at home and abroad; corresponding calculation methods and design theories were initially formed as well [24–26].

However, the CFST members with normal sections have gradually failed to meet the demands of actual engineering projects with improvements in modern society's requirements for architectural appearance aesthetics and structural efficiency. Therefore, an array of special-shaped steel tubular sections (such as fan-shaped [27], L-shaped [28], octagon [29], etc.) emerges as the times require. Among these, the tube with an elliptical section is considered as a kind of novel, high-performance and efficient member due to its combined advantages of circular and square steel tubes [30,31]. Because of its superiorities in terms of flexible primary and secondary axis distribution, good aesthetic appearance and small flow resistance, it has been generally adopted by important public projects, such as airport terminals, large-span spaces, large bridges and high-buildings, in recent years [32], as shown in Figure 1.

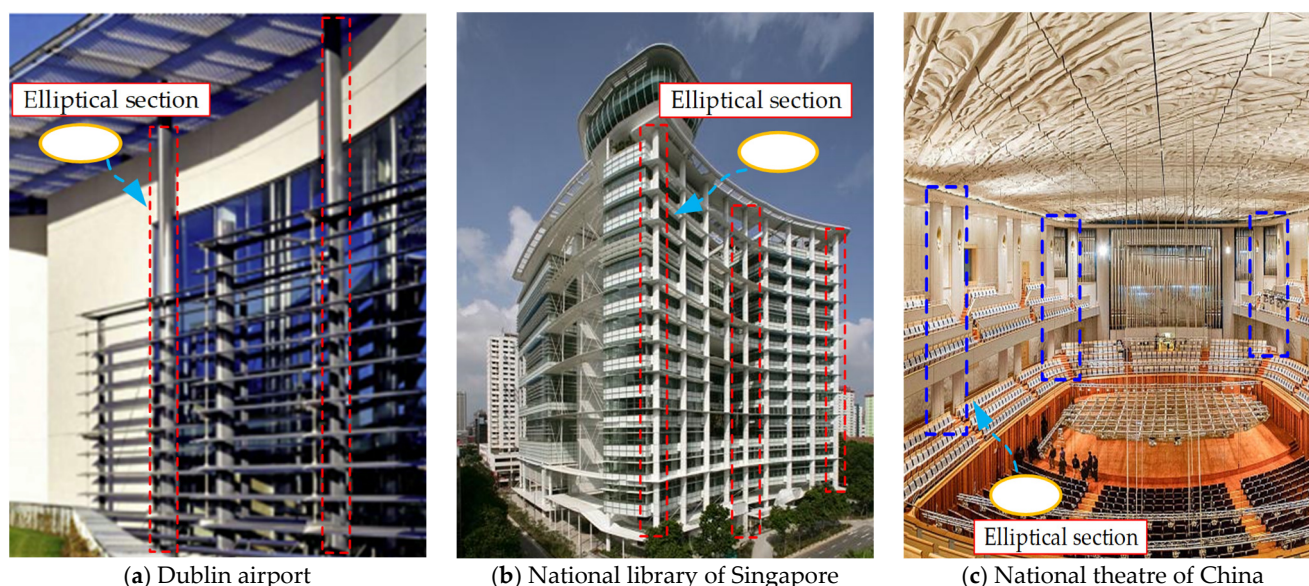


Figure 1. The application of elliptical steel tube.

In view of the increasing engineering demands, some scholars and engineers successfully performed a sequence of experimental studies, numerical modelling and theoretical analyses on the structural responses of concrete-filled elliptical steel tubular (CFEST) members. For example, Yang et al. [33,34], Dai and Lam [35], Mahgub et al. [36], Jamaluddin et al. [37], Liu et al. [38] and Hassanein et al. [39] investigated axially and eccentrically compressed CFEST columns and the feature of confining pressure on the elliptical concrete infills was revealed; moreover, the behaviours of the CFEST members imposed with shear force and bending moment were explored by Ren et al. [40], Zhang et al. [41] and Uenaka and Tsunokake [42,43]. The impressions of the sectional aspect ratio on the responses of the horizontal CFST members with elliptical cross-sections under vertical loads were captured. Following that, the mechanical properties and design recommendations of the CFEST members under single static forces were fostered systematically. Several investigations on the performances of the CFEST members imposed with combined forces (i.e., Shen et al. [32,44], cyclic load [45] and fire exposure [46,47]) were launched as well. All research observed that the CFEST was proven to be one species of composite member with highly artistic

and efficient properties, which was worthy of further application in practical engineering [48–50]. Despite the fact that some scholars carried out a sequence of explorations on the performance of CFEST members imposed with single-static, complex and seismic loads, and the loading responses of CFEST members with circular and rectangular sections were captured and summarized, while relative explorations on the mechanical behaviours of CFEST members with elliptical cross-sections are hardly observed, further extensive application of elliptical steel tubes in practical engineering is quite limited.

In an effort to figure out the CFEST members with high-efficient elliptical steel hollow sections, this paper firstly intends to launch a laboratory test of axial-compressed concrete-filled double-skin elliptical steel tubular (CFDEST) short columns and develop a finite element (FE) analysis model, considering the influence of elliptical section characteristics and hollow ratio. The parameters' influence (i.e., hollow ratio, diameter-to-thickness ratio, and long-short axis ratio) on the failure morphology, load-bearing capacity, initial rigidity and interface interaction of the axially compressed CFDEST short columns is systematically investigated. The calculation formulae of axial compress capacity of CFDEST short columns, considering the impressions of hollow ratio and elliptical cross-section characteristics, are proposed preliminarily. The research results may furnish a scientific basis for applying the CFDEST members in practical engineering. The methodology of this study is shown in Figure 2.

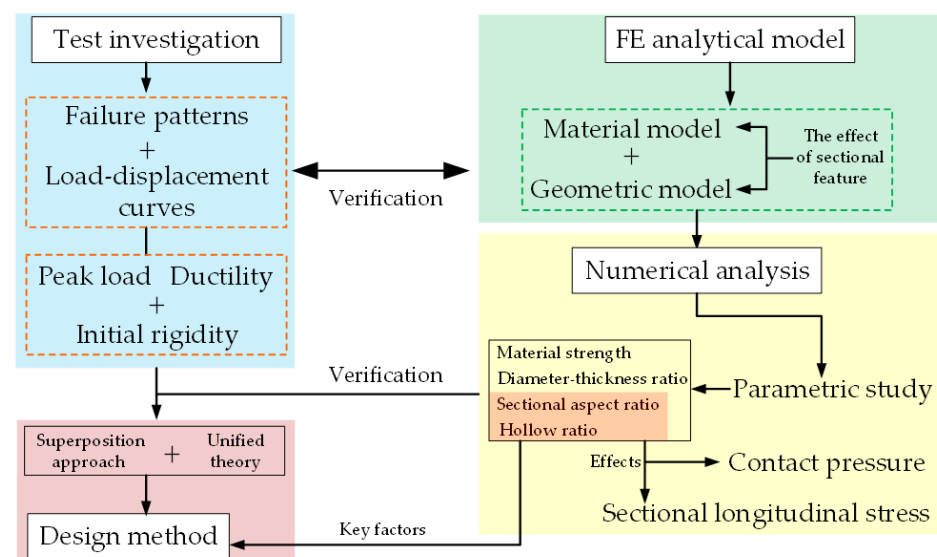


Figure 2. The methodology of this study.

2. Experimental Program

2.1. Specimen Design

In this laboratory test, a total of 10 short column specimens was designed, including two elliptical hollow steel tubular (EHSS) short column specimens, two CFEST short column specimens and six CFDEST short column specimens. The sectional dimension of the outside elliptical steel tube (EST) is $280 \text{ mm} \times 140 \text{ mm} \times 6 \text{ mm}$ ($2a_o \times 2b_o \times t_o$, where $2a_o$ and $2b_o$ stands for the long and short axis' outer diameters of the outside EST, t_o represents the thickness of the outside EST). Similarly, the sectional dimension of the inside EST is $95 \text{ mm} \times 53 \text{ mm} \times 4 \text{ mm}$ ($2a_i \times 2b_i \times t_i$, where $2a_i$ and $2b_i$ stands for the long and short axis' outer diameters of the inside EST, t_i represents the thickness of the inside EST). In order to ensure that the test specimen is a short column and eliminate the impact of the loading plate constraint state on the section stress of the CFDEST column, the column height L is taken as 500 mm according to the provisions of Ref. [51], where $L/(2b_o)$ is about 3.5. Details of the specimens are shown in Figure 3 and Table 1.

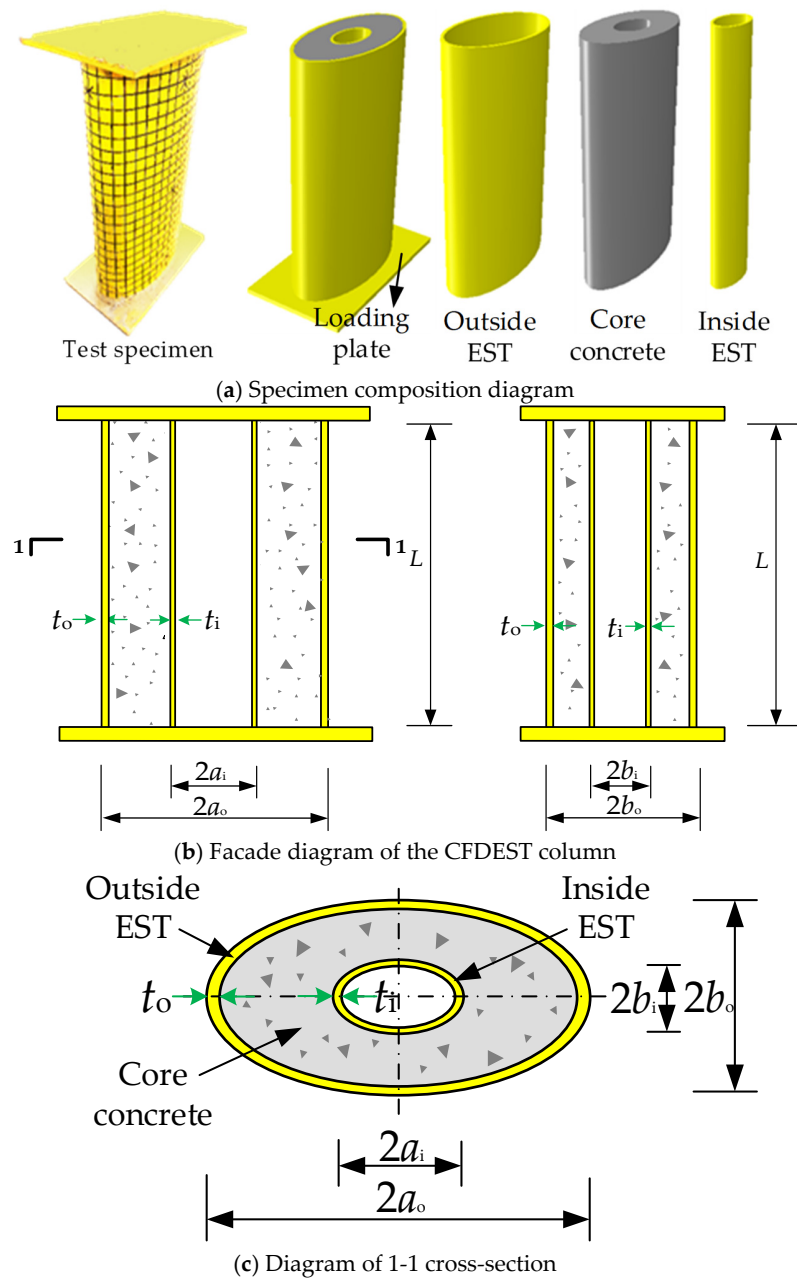


Figure 3. The design diagram of the CFDEST short column.

Table 1. The information of test specimens.

Specimen ID	$2a_o \times 2b_o \times t_o/\text{mm}$	$2a_i \times 2b_i \times t_i/\text{mm}$	f_{yo}	f_{yi}	f_{cu}
SEH-S2	$280 \times 140 \times 6$	—	270.3	—	—
SEH-S4	$280 \times 140 \times 6$	—	421.5	—	—
SE-S2	$280 \times 140 \times 6$	—	270.3	—	58.3
SE-S4	$280 \times 140 \times 6$	—	421.5	—	58.3
DE-S44-C1	$280 \times 140 \times 6$	$95 \times 53 \times 4$	421.5	433.7	38.6
DE-S42-C1	$280 \times 140 \times 6$	$95 \times 53 \times 4$	421.5	276.2	38.6
DE-S22-C1	$280 \times 140 \times 6$	$95 \times 53 \times 4$	270.3	276.2	38.6
DE-S44-C2	$280 \times 140 \times 6$	$95 \times 53 \times 4$	421.5	433.7	58.3
DE-S42-C2	$280 \times 140 \times 6$	$95 \times 53 \times 4$	421.5	276.2	58.3
DE-S22-C2	$280 \times 140 \times 6$	$95 \times 53 \times 4$	270.3	276.2	58.3

Note: f_{yo} , f_{yi} and f_{cu} represent the measured yield stress values of outside EST, inside EST and cubic compressive strength of concrete, respectively (unit: MPa).

2.2. Material Property

Four different types of EST were used in the specimens, which were transformed from circular hot-finished steel tubes with yield strengths of 235MPa and 345MPa via a cold-forming process. Therefore, the curvature of each point in the elliptical section is different. To capture the properties (average yield strength (f_y), ultimate strength (f_u), yield strain (ϵ_y), elastic modulus (E_s) and elongation (δ), etc.) of the EST, the material test for the tensile coupons at three different positions (i.e., major-axis endpoint (point 1), minor-axis endpoint (point 3) and 1/4 arc midpoint (point 2)) in each EST's 1/4 arc was conducted based on the specification GB/T 2975-2018 [52]. Details on the sample locations and coupon test findings are revealed in Figure 4 and Table 2.

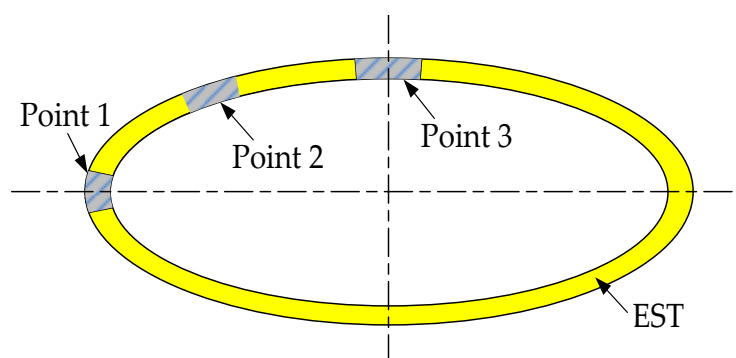


Figure 4. The positions of the tensile coupons.

Table 2. The results of steel coupon test.

ID	f_y /MPa	f_u /MPa	ϵ_y /%	E_s /MPa	δ /%
S-a	270.3	368.9	0.31	203.6	23.5
S-b	421.5	485.6	0.37	205.8	21.1
S-c	276.2	352.8	0.31	202.1	24.2
S-d	433.7	491.1	0.38	206.2	20.6

Note: 'S-a' and 'S-b' respectively represents the test coupons of ESTs with a cross-section of $280 \times 140 \times 6$ mm, which are cold-formed by hot-finished circular steel tube with nominal yield strength of 235 MPa and 345 MPa; 'S-c' and 'S-d' respectively represents the test coupons of with a cross-section of $95 \times 53 \times 4$ mm, which are cold-formed by hot-finished circular steel tube with nominal yield strength of 235 MPa and 345 MPa.

Two kinds of concrete infills having nominal cubic compressive strengths of 30 MPa and 60 MPa were used for the specimens' concrete infills. Three $150 \text{ mm} \times 150 \text{ mm} \times 150 \text{ mm}$ standard cube blocks and three $150 \text{ mm (height)} \times 150 \text{ mm (width)} \times 550 \text{ mm (length)}$ prism blocks were produced by the same batch of concrete. The material properties of the various concrete infills were tested according to specification GB/T 50081-2019 [53] after curing for 28 days. The average cubic compressive stresses of the infilled concrete were 36.8 MPa and 58.3 MPa and their average elastic rigidity was 24,062.5 MPa and 32,060.4 MP.

2.3. Loading Device and Measurement Content

The axial pressure was exposed to the test specimens via a 500Tonner multifunctional hydraulic servo testing machine. A 500Tonner pressure sensor was adopted to capture the axial force. Moreover, the load and displacement hybrid control loading procedure were utilized. Before the formal test, the sensors, loading heads, specimens, displacement meters and other devices and equipment are aligned by laser level and plumb line. At the same time, the sensitivity of the test equipment and acquisition instrument is calibrated by preloading. During the formal loading, the force control step loading procedure was adopted before the pressure force touched the estimated peak load (N_u) of the specimen. Before the axial load arrived at $0.8 N_u$, each loading stage exercised 100 kN per minute to the specimen and then kept constant for about 90 s. After the axial force exceeded $0.8 N_u$,

each loading stage exercised 50 kN per minute to the specimen and then kept constant for about 120 s. After the axial load reaches N_u , the displacement-control step loading procedure was adopted, each loading stage exerted 0.1mm displacement per minute and the force and displacement responses were collected in real time. The loading procedure would be stopped until the pressure load declined down to 0.85-times peak force. Detailed loading and measurement devices are illustrated in Figure 5.

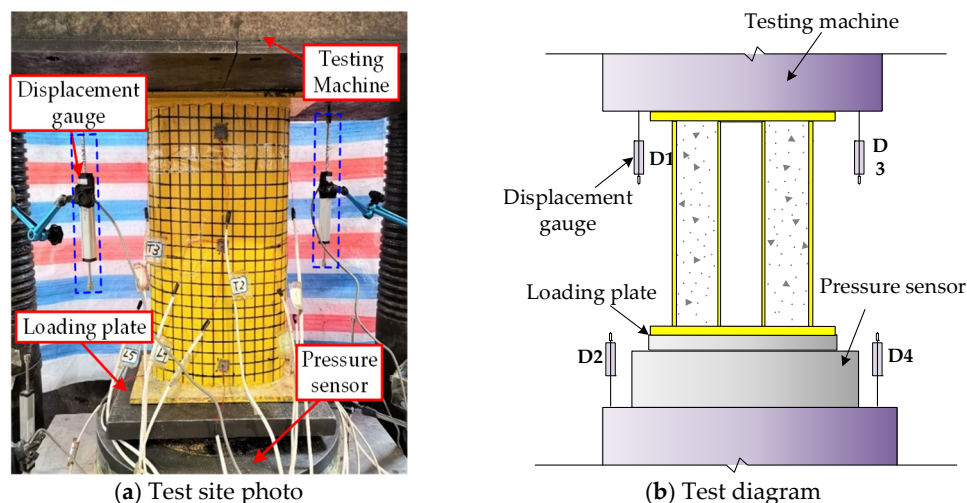


Figure 5. The loading and measurement devices of the test.

3. Test Results and Analyses

3.1. Failure Patterns

For the specimens with zero hollow ratios (named CFEST columns), the experimental outcomes revealed that their failure morphologies were mainly manifested as the outward local bulges of the outside EST and the oblique brittle shear failure of the infilled concrete. At the same time, the oblique shear plane of the concrete infills mainly developed along the weak axis direction, which may be induced by the inferior confinement at the smaller curvature part of the elliptical cross-section. On the other hand, when the hollow ratio reached 100% (named EST short column), the steel tube lacked the effective support originating from the core concrete; hence, the steel tube showed obvious inward depression failure mode (seen in Figure 6a).

With respect to the axially compressed CFDEST stub columns, their failure patterns included the local buckling of the outside EST, the local depression of the inner EST and the crushing of the core concrete, etc., as shown in Figure 6b. Compared with the CFEST specimens, the brittle shear failure of the inside core concrete is inhibited thanks to the good confining effect furnished by the inside and outside ESTs; therefore, the crushing of the concrete on a certain cross-section finally appeared under the high axial compression stress. In addition, the inside EST could only bulge inward to the hollow side by virtue of the outside support provided by the concrete infills.

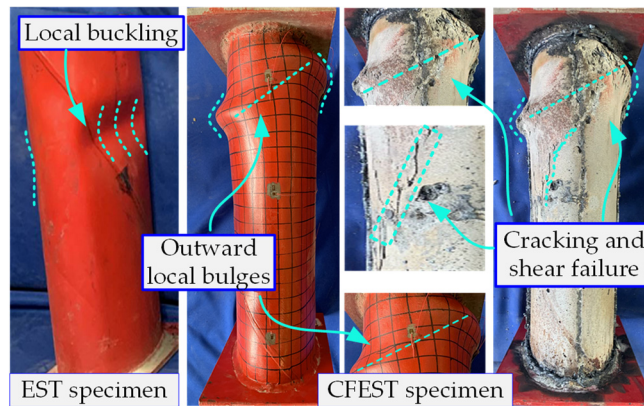
3.2. Axial Pressure versus Axial Displacement Curves

The axial pressure versus axial displacement ($N-\Delta$) curve was recorded during the test process (shown in Figure 7) and the following findings were found:

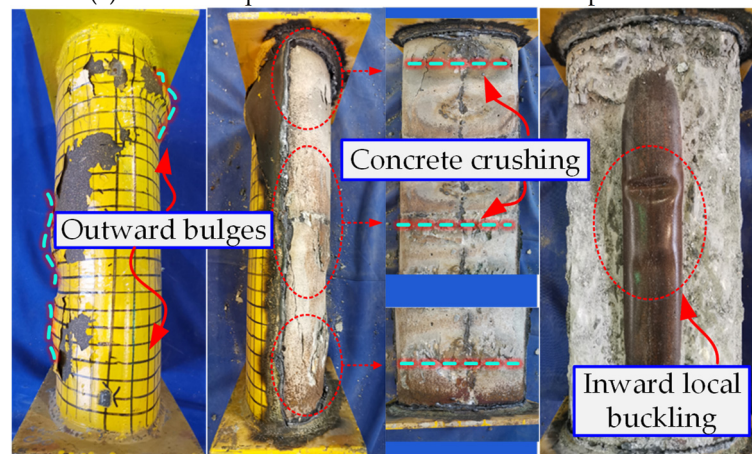
- (1) Due to the lack of a core concrete support effect, the $N-\Delta$ curves of the EST specimens displayed an obvious and rapid decline trend after their peak loads. Similarly, an obvious descent was also observed in $N-\Delta$ relationships of the CFEST short columns, owing to their brittle shear failure of the inside concrete infills.
- (2) Along with an increment in hollow ratio, the sectional area and initial rigidity of the test specimen gradually decreased. However, due to the good confining effect of the inside and outside ESTs on the inside core concrete, the brittle characteristics of the

plain concrete were effectively suppressed and the descending section of the $N-\Delta$ curve was gentler.

- (3) The increment in steel material strength barely offered any effect on the curve's initial rigidity and decreasing segment of the CFDEST short column. Accompanied by an increment in concrete yield stress, the initial rigidity of the axially compressed CFDEST short column was improved. However, because the brittle characteristics of concrete would become more obvious along with the improvement in strength, the slope of the decline section of the $N-\Delta$ relationship was heightened.



(a) The failure patterns of the EST and CFDEST specimens



(b) The failure patterns of the CFDEST patterns

Figure 6. The typical failure of the test specimens.

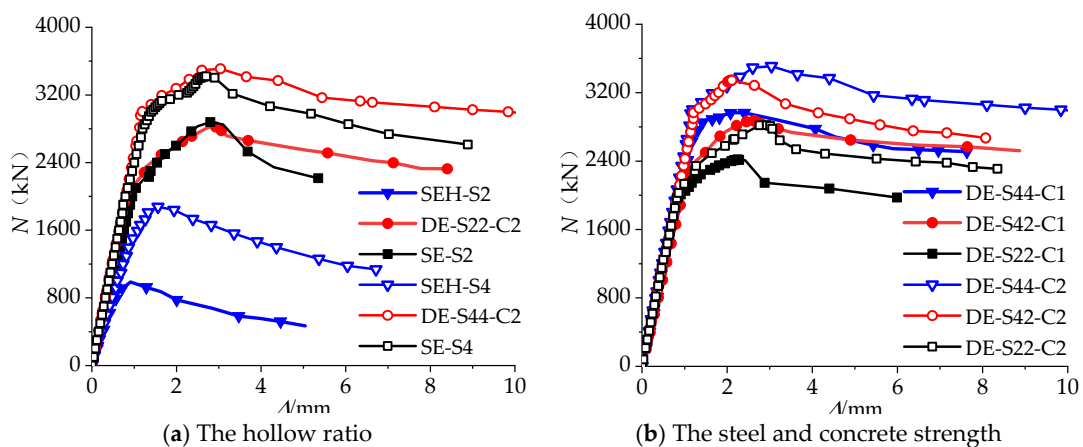


Figure 7. The $N-\Delta$ curves of the specimens.

3.3. The Peak Load and Initial Rigidity

According to the N - Δ curves in Figure 7, the peak loads (N_{ut}) and initial rigidity (K_i) of the specimens can be determined and detailed findings can be seen in Table 3, based on comparison and analysis:

- (1) Compared with the axially compressed CFEST short columns, although the sectional area of the CFDEST short columns decreased by about 10.0%, their axial peak loads were not weakened. For instance, the initial rigidity of specimens DE-S44-C2 and DE-S22-C2 was, respectively, 26.6% and 22.7% lower than that of specimens SE-S4 and SE-S2, while the differences in axial peak load were only 0.3% and 3.6%. This may be attributed to the excellent confinement on the inside core concrete furnished by the outside and inside ESTs.
- (2) Since the cross-sectional area value of the outside EST is much larger than that of the inside EST, the impression of strength improvement outside EST on the axial peak force of the CFDEST stub column is much greater than that of the inside EST. When the strength of the outside EST changed from 421.5 MPa to 270.3 MPa, the axial peak loads of the specimens DE-S22-C1 and DE-S22-C2 were, respectively, 18.8% and 18.5% lower than those of specimens DE-S42-C1 and DE-S42-C2. On the condition that the strength of the inside EST increased from 270.3 MPa to 421.5 MPa, the axial peak loads of the specimens DE-S44-C1 and DE-S44-C2 were only 3.2% and 5.0% higher than those of specimens DE-S42-C1 and DE-S42-C2, respectively.
- (3) The results indicated that the axial peak pressure and initial rigidity of the CFDEST short column were highly improved along with the enhancement in concrete stress. The axial peak loads of specimens DE-S44-C2, DE-S42-C2 and DE-S22-C2 ($f_{cu} = 58.3$ MPa) were, respectively, 18.3%, 16.3% and 16.6% higher than those of specimens DE-S44-C1, DE-S42-C1 and DE-S22-C1 ($f_{cu} = 38.6$ MPa) and the initial rigidity increased 11.1%, 13.6% and 12.1% correspondingly.

Table 3. The test results.

Specimen ID	Δ_y /mm	$\Delta_{0.85}$ /mm	DI	K_i /kN·mm ⁻¹	N_{ut} /kN
SEH-S2	0.65	1.39	2.14	1505.8	985
SEH-S4	1.09	3.57	3.28	1730.2	1881
SE-S2-C2	0.84	3.63	4.32	3233.7	2723
SE-S4-C2	1.03	5.42	5.26	3405.2	3501
DE-S44-C1	1.32	7.63	5.78	2250.1	2966.8
DE-S42-C1	1.31	7.42	5.42	2200.3	2874.4
DE-S22-C1	1.08	5.12	5.07	2230.1	2419.6
DE-S44-C2	1.40	7.84	5.60	2500.2	3510.2
DE-S42-C2	1.34	7.29	5.24	2499.9	3344.3
DE-S22-C2	1.13	5.56	4.92	2500.0	2822.0

Note: Δ_y stands for the axial displacement corresponding to test specimens' yield strength, as defined in [30]; $\Delta_{0.85}$ represents the axial displacement corresponding to the axial force declines to 0.85 times of the measured peak force [30].

3.4. Ductility Index

The ductility indexes (DI) of the specimens were calculated and analysed in this section [30], which can be calculated as follows:

$$DI = \Delta_{0.85} / \Delta_y \quad (1)$$

As shown in Table 3, some observations can be concluded as follows:

- (1) Compared with specimens SEH-S2 and SEH-S4, the DI s of specimens SE-S2-C2 and SE-S4-C2, respectively, increased 101.9% and 60.4%. This phenomenon is caused by the support action furnished by the inside core concrete infills; hence, the local buckling behaviour is inhibited and the ductility of the column is significantly improved.

- (2) Compared to the specimens SE-S2-C2 and SE-S4-C2, the specimens DE-S22-C2 and DE-S44-C2, respectively, offered increments of 13.9% and 6.5% in *DIs*, which are induced by the excellent support effect stemming from outside and inside steel tubes.
- (3) The *DIs* of specimens DE-S44-C1, DE-S42-C1 and DE-S22-C1 were, respectively, 3.2%, 3.4% and 3.0% higher than those of specimens DE-S44-C2, DE-S42-C2 and DE-S22-C2. The comparison reflected that the *DI* of the axially compressed CFDEST stub column decreased with the increase in concrete strength, due to the brittle feature of the inside concrete with higher compressive strength.

4. Numerical Analyses

Since the time and economic costs of the experimental study are difficult to control, to carry out the research work in a careful and efficient way, it is necessary to establish a numerical model of the axially compressed CFDEST stub column in light of the current mature FE analysis technology.

4.1. FE Modelling

The FE analysis model is mainly composed of the material model and geometric model. The following descriptions are the details.

4.1.1. Material Model

According to the composition of the test specimen, the material model of the CFDEST short column involves core concrete, inside and outside steel tubes and end-loading plates.

In terms of the infilled concrete, a constitutive relationship model for simulating its stress–strain development rule is recommended and adopted by many studies [34,38] in line with a collection of experimental and theoretical analyses (seen in Figure 8a). The model can be expressed as follows:

$$y = \begin{cases} 2x - x^2 & x \leq 1 \\ x / [\beta_0(x - 1)^\eta + x] & x > 1 \end{cases} \tag{2}$$

$$\beta_0 = 0.5 \times (2.36 \times (a/b)^5 \times 10^{-5})^{[0.25 + (\xi - 0.5)^2]} f_c^{0.5} \geq 0 \tag{3}$$

in which, $x = \epsilon/\epsilon_0$, $y = \sigma/f_c$, ϵ and σ denote the strain and stress of the inside concrete infills; f_c denotes the concrete’s cylinder compressive strength; a and b denote the sizes of the semi-major and semi-minor axes. More details on the definitions of the characters can be found in the literature [34,38].

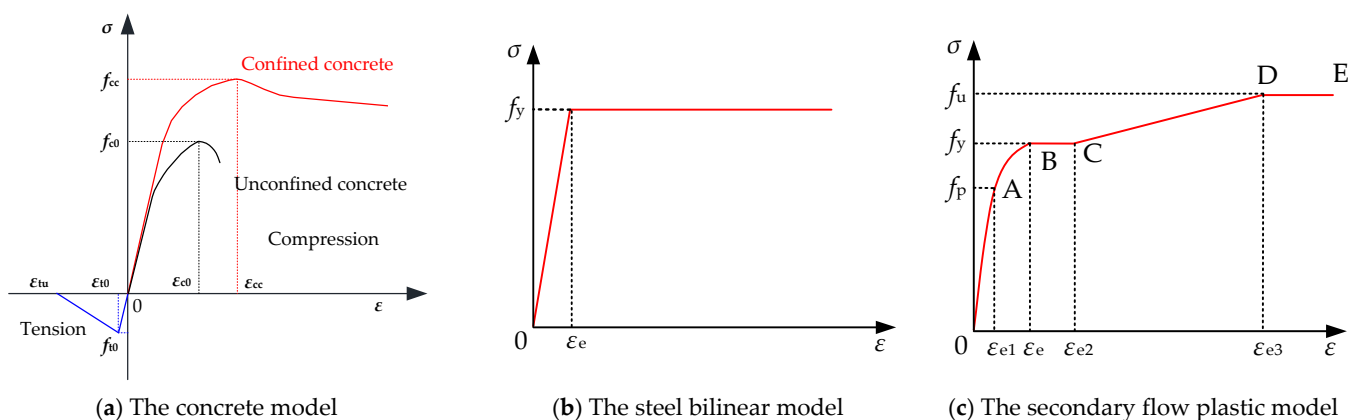


Figure 8. Stress–strain relationships of the steel and concrete.

For the inside and outside steel tubes of the specimens, the bilinear model suggested by Ref. [30] is utilized because of the cold-forming production approach, whereas the

secondary flow plastic model [15] is used to reflect the responses of the upper and lower loading plates since they are made of low-carbon hot-rolled steel. Details are illustrated in Figure 8b,c.

4.1.2. Geometric Model

The geometric model mainly includes element types, contact interaction and boundary conditions.

In terms of the loading end plates and infilled concrete, the three-dimensional solid (C3D8R) element is adopted [30,54]. For the outside and inside ESTs, the element node number following the thickness direction is limited by employing the C3D8R element due to the thin-walled characteristic of the EST, which affects the accuracy of the simulation in turn. Therefore, the shell element (S4R) is preferred to apply for simulating the inside and outside ESTs [30].

The interactions between various components contain the steel-to-concrete interaction and the steel-to-steel interaction. The ‘tie’ option is employed to simulate the welding between the inside/outside ESTs and the loading plates [30], while the ‘surface-to-surface’ contact action is suggested to reflect the interactions of ESTs-to-concrete and loading plate-to-concrete, which includes the behaviour in tangential and normal directions [38]. For normal behaviour, ‘hard’ contact is adopted. Tangential behaviour adopts the ‘coulomb friction model’ and the coefficient value of the friction is usually taken as 0.6 according to some relevant research [54,55].

The boundary conditions are set by coupling to the outside surfaces of the loading end plates. To reflect the actual boundaries of the test specimens, the fixed condition is applied for the lower loading plate and the freedoms of all displacements and rotations are limited. The axial compression force is exposed to the test specimen through the upper loading plate. To ensure uniform axial compression on the loading plate, a reference point (RP) coupling to the upper surface of the top loading end plate is used and the axial displacement force is attached to the RP along the z-axis direction. The specific finite element analysis model is shown in Figure 9.

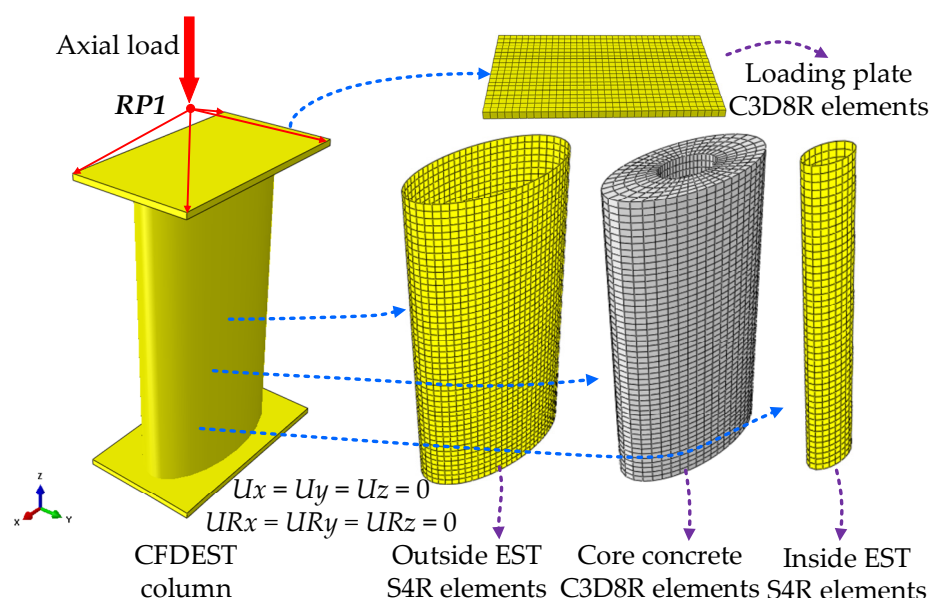


Figure 9. Finite element model of the axially compressed CFDEST short column.

4.2. Test Validation

Based on the above description, the validation of the numerical model on the CFDEST stub column imposed with axial pressure is launched by comparing the simulation results with the axial pressure–axial displacement relationships and failure morphologies of the

experiments, as shown in Figures 10 and 11. The outcomes declare that the outward bulges of the outside EST, the inward depression of the inside EST and the crushing of the core concrete reflected in the FE models coincide well with the test outcomes. Their axial load-bearing capacities and load–displacement curves are in good agreement as well. The average value of predicted axial resistances versus experimental peak forces (N_{FE}/N_t) is 1.03 and the error is only 9.41%. Therefore, the comparison outcomes deliver that the FE analytical model of axially compressed CFDEST stub columns established in this article has good accuracy and reliability, which can be used to further investigate the mechanical performance in detail.

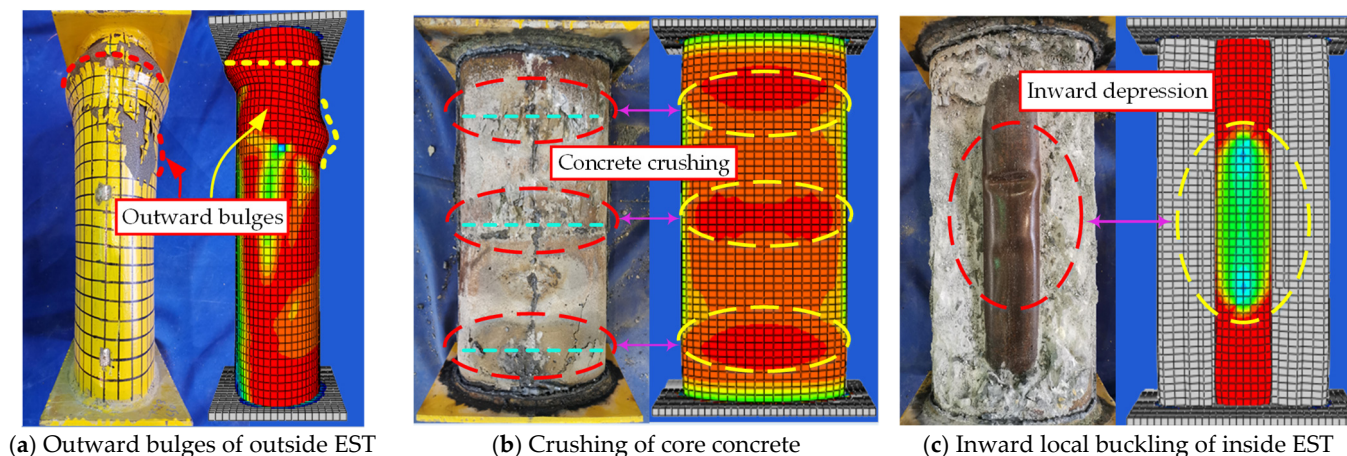


Figure 10. Comparison on failure modes between test and FE model.

4.3. Parametric Analysis

To systematically study the performance of the axially compressed CFDEST stub column, the impact of various parameters on the load-bearing capacities and the initial rigidity and ductility index was studied. The parameters mainly contain: (1) material parameters: the yield stresses of inside and outside ESTs ($f_y = 235\sim 460$ MPa), the strength of the core concrete ($f_{cu} = 30\sim 100$ MPa); (2) geometric parameters: hollow ratio ($\chi = a_i b_i / (a_o b_o) = 10\sim 50\%$), diameter-to-thickness ratio ($\alpha = 2a_o / t_o$) and section aspect ratio (a_o / b_o). Detailed information on FE models and calculation results is shown in Table 4 and Figure 12.

In light of the analytical outcomes in Table 4 and Figure 12, the following findings can be drawn as:

- (1) The peak force of the axially compressed CFDEST stub column is enhanced by the increments in steel and concrete strengths and declined with the increasing hollow ratio, diameter/thickness ratio and sectional aspect ratio;
- (2) The initial rigidity of the axially compressed CFDEST short column grows with the increase in concrete stress and decreases with the increments in sectional hollow ratio and diameter/thickness ratio. However, the steel strength and the sectional aspect ratio barely have any effect on the initial rigidity;
- (3) The ductility index of the column decreases with the increments in concrete strength, diameter/thickness ratio, hollow ratio and sectional aspect ratio.

4.4. Contact Pressure

To further clarify the interaction characteristics between the EST and the inside core concrete, the contact pressure of the axially compressed CFDEST short column under axial compression is extracted in line with the above FE analysis. The impression of the sectional hollow ratio and the elliptical section characteristics on the contact stress is revealed, as shown in Figure 13. Points 1~4 are the equipartition points of the 1/4 elliptical arc at the interface between outside EST and core concrete, which are numbered from major axis end point to the minor axis end point; Points a~c are the bisection points of 1/4 elliptical arc at

the interface between inside EST and core concrete, point a represents the major-axis end point, point c represents the minor-axis end point.

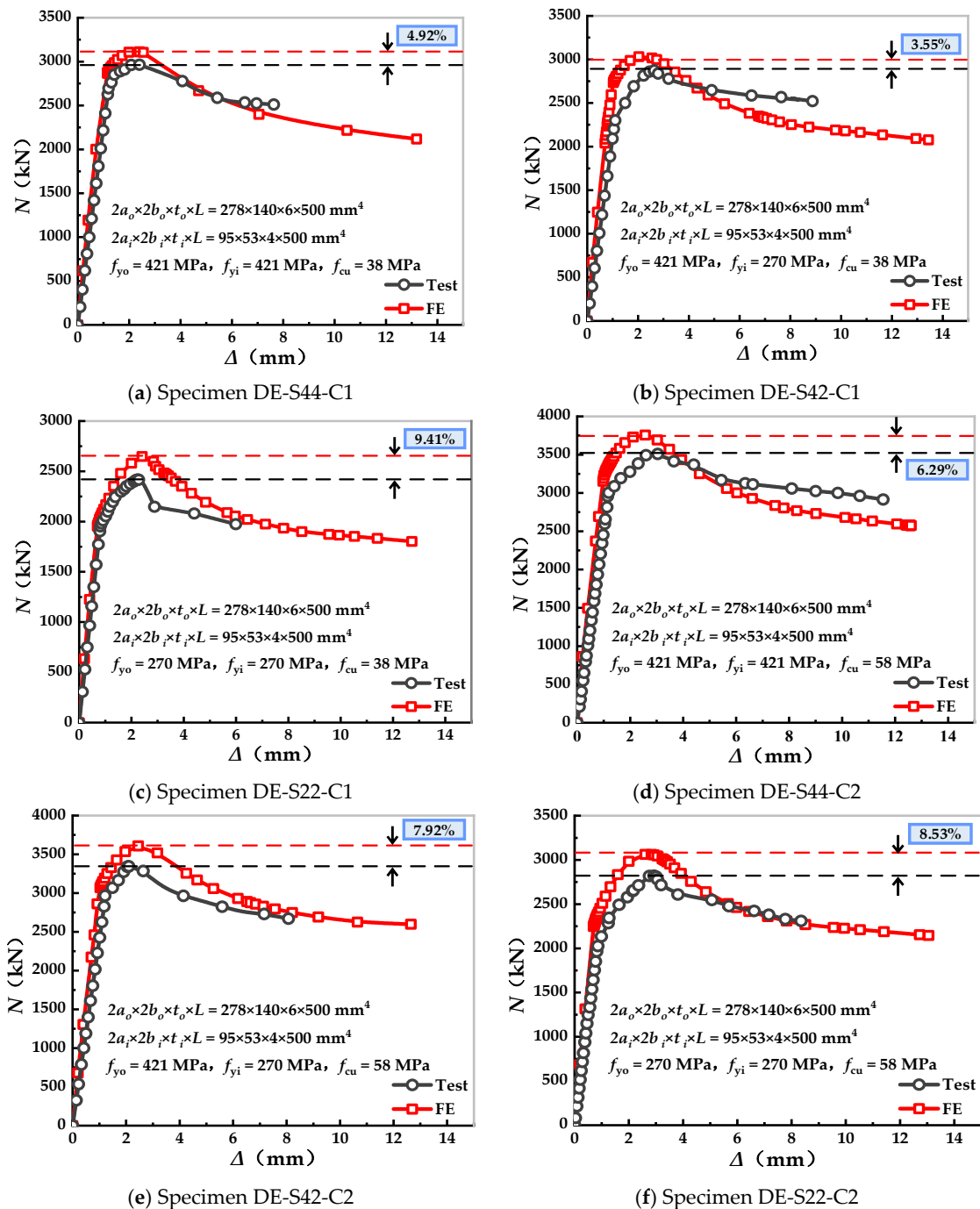


Figure 11. Comparison on force–displacement curves between test and FE model.

Table 4. Information and calculation results of the FE models.

Parameters	Specimen ID	$2a_o \times 2b_o \times t_o \times L$	$2a_i \times 2b_i \times t_i \times L$	f_{yo}	f_{yi}	f_{cu}	χ	N_u	K_i	$\Delta_{0.85}$	DI
Steel strength	CFDEST-fy-1	$400 \times 200 \times 8 \times 600$	$160 \times 80 \times 4 \times 600$	355	355	50	15%	5829.4	4754.1	5.68	4.63
	CFDEST-fy-2	$400 \times 200 \times 8 \times 600$	$160 \times 80 \times 4 \times 600$	355	460	50	15%	5997.4	4754.1	5.83	4.62
	CFDEST-fy-3	$400 \times 200 \times 8 \times 600$	$160 \times 80 \times 4 \times 600$	460	355	50	15%	6573.8	4754.1	5.67	4.10
	CFDEST-fy-4	$400 \times 200 \times 8 \times 600$	$160 \times 80 \times 4 \times 600$	460	460	50	15%	6735.8	4754.1	5.88	4.15
	CFDEST-fy-5	$400 \times 200 \times 8 \times 600$	$160 \times 80 \times 4 \times 600$	355	235	50	15%	5634.0	4754.1	5.76	4.86
	CFDEST-fy-6	$400 \times 200 \times 8 \times 600$	$160 \times 80 \times 4 \times 600$	235	355	50	15%	5005.1	4754.1	5.49	5.21
	CFDEST-fy-7	$400 \times 200 \times 8 \times 600$	$160 \times 80 \times 4 \times 600$	235	235	50	15%	4809.7	4754.1	5.59	5.53
Concrete strength	CFDEST-fc-1	$400 \times 200 \times 8 \times 600$	$160 \times 80 \times 4 \times 600$	355	355	30	15%	4903.9	4276.9	6.11	5.33
	CFDEST-fc-2	$400 \times 200 \times 8 \times 600$	$160 \times 80 \times 4 \times 600$	355	355	40	15%	5372.7	4518.3	5.91	4.97
	CFDEST-fc-3	$400 \times 200 \times 8 \times 600$	$160 \times 80 \times 4 \times 600$	355	355	60	15%	6269.7	4989.3	5.68	4.52
	CFDEST-fc-4	$400 \times 200 \times 8 \times 600$	$160 \times 80 \times 4 \times 600$	355	355	70	15%	6695.1	5216.2	5.51	4.29
	CFDEST-fc-5	$400 \times 200 \times 8 \times 600$	$160 \times 80 \times 4 \times 600$	355	355	80	15%	7106.0	5433.2	5.46	4.17
	CFDEST-fc-6	$400 \times 200 \times 8 \times 600$	$160 \times 80 \times 4 \times 600$	355	355	90	15%	7503.7	5644.2	5.53	4.16
	CFDEST-fc-7	$400 \times 200 \times 8 \times 600$	$160 \times 80 \times 4 \times 600$	355	355	100	15%	7888.4	5846.9	5.54	4.11
Hollow ratio	CFDEST- χ -1	$400 \times 200 \times 8 \times 600$	$120 \times 60 \times 4 \times 600$	355	355	50	10%	6059.4	4783.0	5.46	4.31
	CFDEST- χ -2	$400 \times 200 \times 8 \times 600$	$180 \times 90 \times 4 \times 600$	355	355	50	20%	5715.7	4724.2	5.65	4.67
	CFDEST- χ -3	$400 \times 200 \times 8 \times 600$	$220 \times 110 \times 4 \times 600$	355	355	50	30%	5400.3	4630.3	5.68	4.87
	CFDEST- χ -4	$400 \times 200 \times 8 \times 600$	$250 \times 125 \times 4 \times 600$	355	355	50	40%	5127.3	4528.4	5.79	5.11
	CFDEST- χ -5	$400 \times 200 \times 8 \times 600$	$280 \times 140 \times 4 \times 600$	355	355	50	50%	4809.6	4403.3	5.71	5.23
Diameter-to-thickness ratio	CFDEST- α -1	$400 \times 200 \times 8 \times 600$	$160 \times 80 \times 3 \times 600$	355	355	50	15%	5726.1	4628.4	5.53	4.47
	CFDEST- α -2	$400 \times 200 \times 6 \times 600$	$160 \times 80 \times 3 \times 600$	355	355	50	15%	5087.9	4106.4	5.19	4.19
	CFDEST- α -3	$400 \times 200 \times 4 \times 600$	$160 \times 80 \times 3 \times 600$	355	355	50	15%	4474.3	3497.3	4.73	3.70
	CFDEST- α -4	$400 \times 200 \times 6 \times 600$	$160 \times 80 \times 4 \times 600$	355	355	50	15%	5195.2	4189.7	5.39	4.35
	CFDEST- α -5	$400 \times 200 \times 4 \times 600$	$160 \times 80 \times 4 \times 600$	355	355	50	15%	4591.8	3623.0	4.56	3.60
Aspect ratio	CFDEST- β -1	$400 \times 200 \times 8 \times 600$	$140 \times 95 \times 4 \times 600$	355	355	50	15%	5803.3	4718.1	5.62	4.57
	CFDEST- β -2	$400 \times 200 \times 8 \times 600$	$115 \times 115 \times 4 \times 600$	355	355	50	15%	5796.2	4699.2	5.90	4.78
	CFDEST- β -3	$360 \times 240 \times 8 \times 600$	$160 \times 80 \times 4 \times 600$	355	355	50	15%	6190.4	4891.9	5.83	4.61
	CFDEST- β -4	$360 \times 240 \times 8 \times 600$	$140 \times 95 \times 4 \times 600$	355	355	50	15%	6164.2	4854.8	5.77	4.54
	CFDEST- β -5	$360 \times 240 \times 8 \times 600$	$115 \times 115 \times 4 \times 600$	355	355	50	15%	6169.5	4839.7	5.99	4.70
	CFDEST- β -6	$300 \times 300 \times 8 \times 600$	$160 \times 80 \times 4 \times 600$	355	355	50	15%	6427.4	4978.4	8.88	6.88
	CFDEST- β -7	$300 \times 300 \times 8 \times 600$	$140 \times 95 \times 4 \times 600$	355	355	50	15%	6678.2	5057.0	/	/
	CFDEST- β -8	$300 \times 300 \times 8 \times 600$	$115 \times 115 \times 4 \times 600$	355	355	50	15%	6712.7	5071.1	/	/

The results show that the distribution rule of the contact stress between the inside core concrete infills and the EST in the axially compressed CFDEST stub column shows obvious inhomogeneity and the contact pressure decreases from the major-axis end point (point 1 or point a) to the minor-axis end point (point 4 or point c) successively. The contact stress between the outside EST and the inside core concrete infills is much larger than that between the inside EST and the infilled concrete. The contact stresses at points a ~c are almost zero at the peak force. The contact pressure of the axially compressed CFDEST stub column at most parts of the cross-section is much smaller than that of the circular CFDST column under the same sectional area, hollow ratio and steel ratio, except the contact pressure located around point 1 (seen in Figure 13a). This phenomenon is initiated because the curvature of the elliptic around the short axis is much smaller than that of the circle, while the curvature of the elliptic around the long axis is much larger.

Meanwhile, with the increments in the sectional hollow ratio, the thickness of the infilled concrete decreases and, therefore, the lateral expansion deformation of the axially compressed concrete gradually decreases. As a result, the contact pressure value between the outside steel tube and the core concrete continues decreasing (shown in Figure 13b).

4.5. Longitudinal Stress Distribution of the Core Concrete

In an effort to further clarify the influence of sectional hollow ratio and elliptical aspect ratio on the longitudinal compressed stress distribution of the concrete cross-section in the axially compressed CFDEST stub column, the models on the effects of hollow ratio (CFDEST- χ -1, CFDEST- χ -3 and CFDEST- χ -1) and aspect ratio (CFDEST-fy-1, CFDEST- β -4 and CFDEST- β -8) are taken as examples to summarize the development rules of the

longitudinal compressed stress at the mid-height concrete section under the axial maximum pressure (seen in Figure 14).

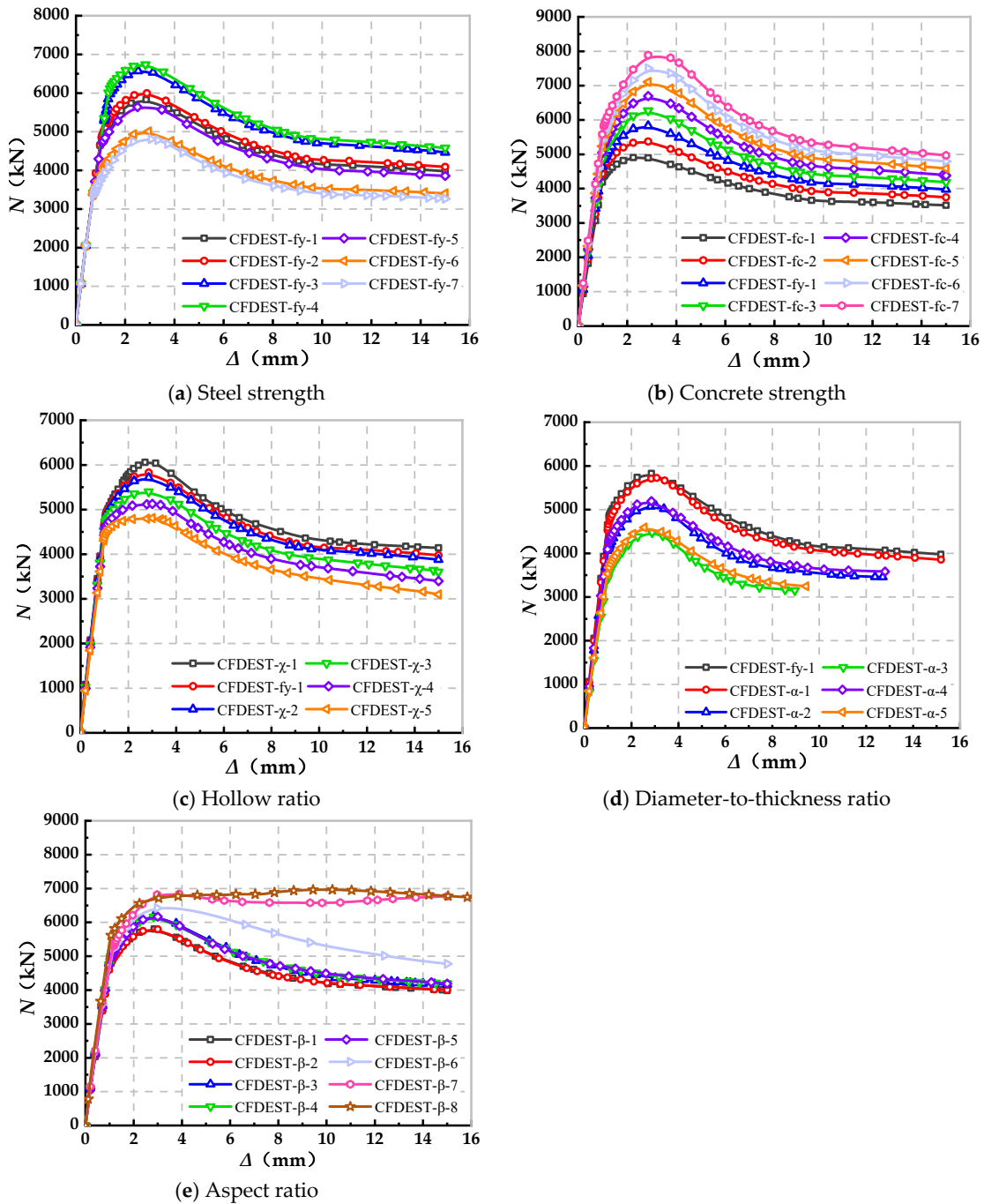
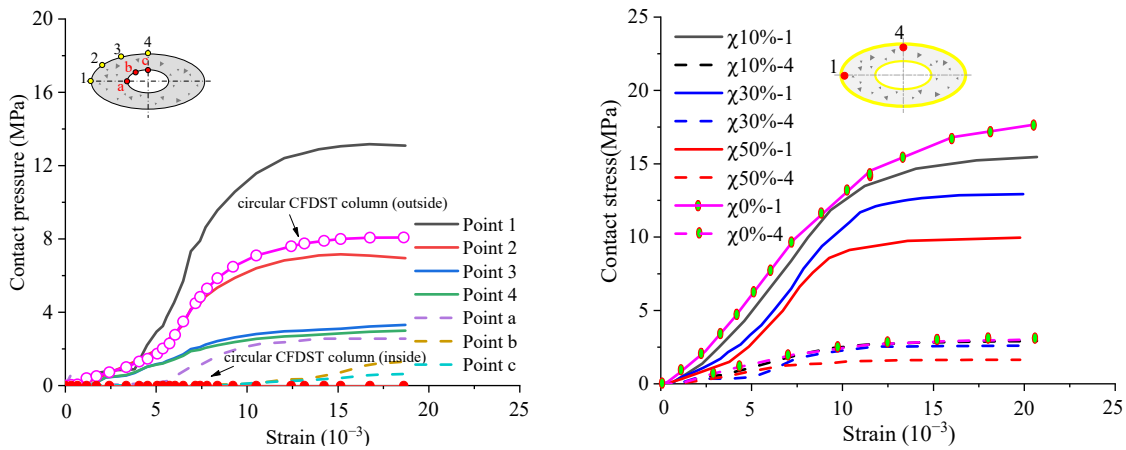


Figure 12. The results of parameter analysis.



(a) The contact stresses at various points (b) The influence of the hollow ratio on contact stress.

Figure 13. Analysis on contact stress of the CFDEST columns under the axial peak loads.

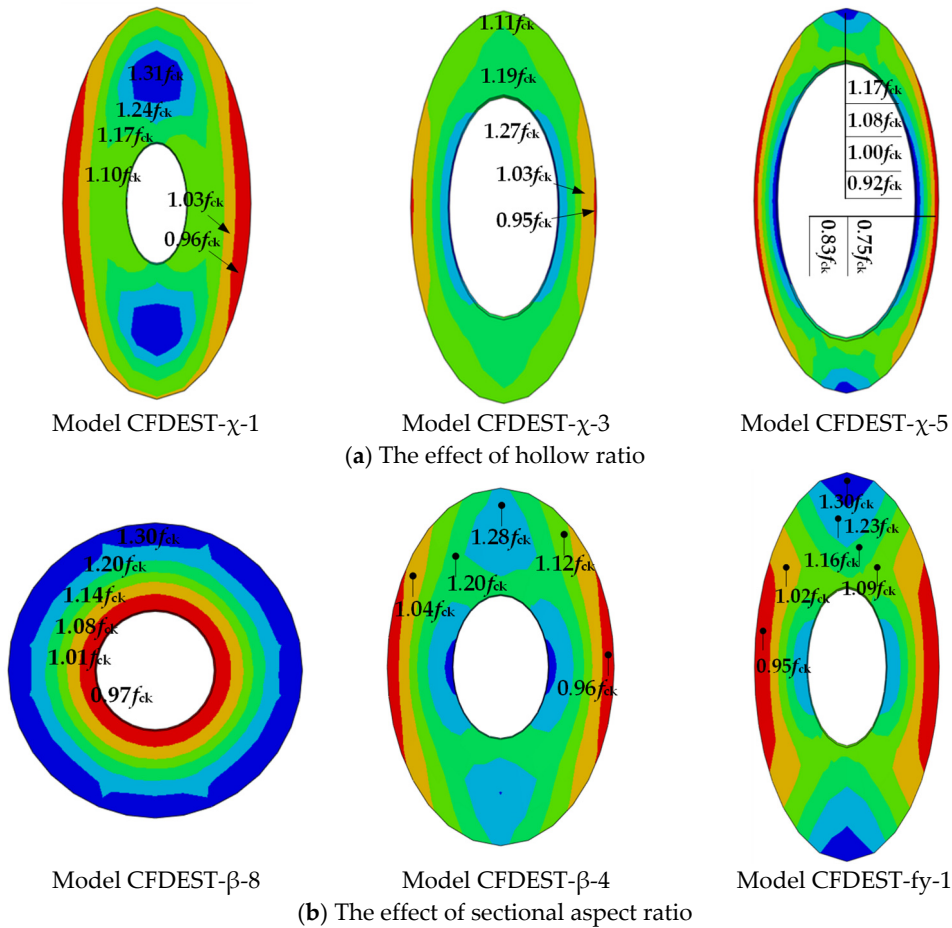


Figure 14. The longitudinal compressed stress of the concrete under the peak force.

The analysis findings are as follows:

- (1) Along with the growth in sectional hollow ratio, the longitudinal compressed stress of the core concrete between two elliptical steel tubular sections decreases gradually. As the analysis in Section 4.4 showed, the growth in the sectional hollow ratio leads to a gradual decrement in the sectional area of the inside concrete infills and, therefore, the expansion value of the inside core concrete infills would be decreased obviously, which will result in a decrease in confining stress between the inside concrete and

outside steel tube. Hence, the peak compressive stress of the inside core concrete decreases accordingly (illustrated in Figure 14a).

- (2) Along with the increment in the sectional aspect ratio, the amplitude of change in curvature at different points of the cross-section grows; therefore, the longitudinal compressed stress distribution of the inside concrete under the maximum pressure load begins to show significant heterogeneity. Based on the results shown in Refs. [30,51], it is known that the average confining stress of CFST column with elliptical cross-section decreases with the growth in the sectional aspect ratio, which leads to a gradual fall in concrete's average longitudinal compressive stress (seen in Figure 14b). The analytical result is consistent with the findings in Section 4.3 and Section 4.4.
- (3) In addition, since both the thickness of the concrete layer and the curvature of the EST keep decreasing from the long-axis end to the short-axis end, the confining stress around the long axis is much higher than that around the short axis. As a consequence, the high longitudinal compressed stress of the concrete mainly locates at the region along the long axis, while the longitudinal compressed stress along the short-axis direction is much smaller.

5. Design Method

Until now, although design recommendations on CFST members have been built up in various national specifications in America [16], Europe [14] and China [17], etc., the calculation formulae on predicting the axial load-bearing capacities of the CFDST members have been seldomly covered, not to mention the CFDST columns with elliptical cross-sections.

5.1. Calculation Formulae

To further encourage the application of CFDEST members in engineering practice, it is quite necessary to provide available calculation formulae to predict their load-bearing capacities properly. In this part, a design recommendation for estimating the load-bearing capacity of the axially compressed CFDEST short column is presented according to the superposition approach [14] and unified theory [15], in which both the feature of elliptical section and the influence of hollow ratio are considered.

Based on the analyses in Section 4, the confinement on the inside concrete is mainly furnished by the outside tube, while the inside tube acts with little constraint effect. Therefore, the outside tube and the inside concrete infills can be treated as one unit in the light of the design suggested by Huang et al. [56] and Han et al. [57], and the inside steel tube is the other unit that shares the axial force separately. Then, the axial compress capacity ($N_{u,c}$) of the CFDEST short column can be described as:

$$N_{u,c} = N_{osc,u} + N_{i,u} \quad (4)$$

in which $N_{osc,u}$ denotes the axial load-bearing capacity provided by the outside tube and inside concrete infills using unified strength theory [15]; $N_{i,u}$ denotes the axial compress capacity contributed by the inside steel tube. The $N_{osc,u}$ and $N_{i,u}$ can be calculated as follows:

$$N_{osc,u} = f_{osc} \times A_{soc} \quad (5)$$

$$N_{i,u} = f_{yi} \times A_{si} \quad (6)$$

$$A_{soc} = A_{so} + A_c \quad (7)$$

in which f_{osc} stands for the unified peak stress of the outside tube and inside concrete infills; f_{yo} , f_{ck} , and f_{yi} , respectively, denote the yield stress of the outside tube, the prism compressed stress of the concrete infills and the yield strength of the inside tube; A_{soc} denotes the sum area of outside tube and infilled concrete; A_{so} , A_c and A_{si} , respectively, denote the cross-section areas of the outside tube, concrete infills and inside tube.

Based on the design rules of axially compressed circular CFDST short columns [58] and the axially compressed CFEST stub columns [38], the f_{osc} can be expressed as follows:

$$f_{osc} = C_1 \chi^2 f_{yo} + C_2 [1.212 + B\bar{\xi} + C\bar{\xi}^2] \times f_{ck} \quad (8)$$

$$B = \left(\frac{0.176 f_{yo}}{213} + 0.974 \right) \left(\frac{b_o}{a_o} \right)^{0.3} \quad (9)$$

$$C = \left(\frac{-0.104 f_{ck}}{14.4} + 0.031 \right) \left(\frac{b_o}{a_o} \right)^{0.3} \quad (10)$$

$$C_1 = \frac{\alpha}{1 + \alpha} \quad (11)$$

$$C_2 = \frac{1 + \alpha_n}{1 + \alpha} \quad (12)$$

$$\alpha = \frac{A_{so}}{A_c} \quad (13)$$

$$\alpha_n = \frac{A_{so}}{A_{ce}} \quad (14)$$

$$A_{ce} = \pi(a_o - t_o)(b_o - t_o) \quad (15)$$

$$\bar{\xi} = \frac{A_{so} f_{yo}}{A_{ce} f_{ck}} \quad (16)$$

in which A_{ce} denotes the sum area of the inside tube and concrete infills; α , α_n stand for the actual and nominal steel ratios of the outside tube; $\bar{\xi}$ denotes the nominal confinement factor of the column. It can be found that the design formulae presented in this section can be back to the calculation method for the axially compressed circular CFDST short column defined in the specification [17], when the sectional aspect ratio equals 1.0. Moreover, on the condition that the hollow ratio becomes zero, the above formulae can be back to the design recommendation of the CFEST short columns shown in Refs. [34,38]. Therefore, the above formulae can be utilized to evaluate the axial compress capacities of the circular CFDST short column and CFEST short column as well.

5.2. Validation

A comparison between the predictions obtained by the design formulae and the results shown in Refs. [31,38,57,58] as well as the test and numerical modelling in this paper are conducted to validate the accuracy and reliability of the expressions. Details can be seen in Figure 15.

The comparison result demonstrates that the average value of evaluation data versus the test and FE results is 0.97 and the variance is 0.003, which means that the prediction obtained by the design formulae agrees well with the test and FE results. Consequently, the design expressions can be used to evaluate the axial compress capacity of the CFDEST short column.

However, it should be noted that the study presented in this paper also has its limitations and scope. In line with the aforementioned experimental and parametric investigations, this study is applicable to the axially compressed CFDEST short columns under the conditions that steel tube yield strength ranges from 235 to 460 MPa, concrete infill compressive strength ranges from 30 to 100 MPa, diameter-to-thickness ratio ranges from 46.7 to 100, hollow ratio ranges from 0 to 50% and sectional aspect ratio ranges from 1.0 to 2.0.

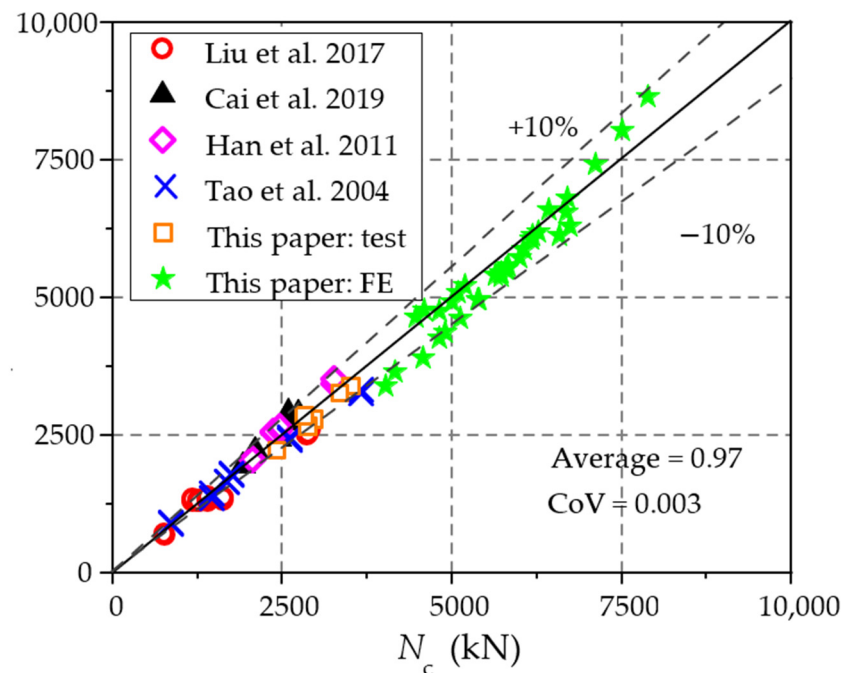


Figure 15. Comparison between predicted data and test and FE results [31,38,57,58].

6. Conclusions

Due to the lack of investigations on the performance of CFDEST members, this paper preliminarily develops an exploration of the behaviour of axially compressed CFDEST short columns via experimental and numerical approaches. The impacts of systematic parameters, including material strength, diameter/thickness ratio, hollow ratio and sectional aspect ratio, are figured out. The development rules of the contact action and concrete longitudinal compress stress correlated to the hollow ratio and sectional aspect ratio are revealed. The calculation formulae to estimate the axial compress capacity of the CFDEST stub column are proposed finally. This article may furnish a scientific basis for the application of CFDEST members. In line with the laboratory tests and numerical analyses of this article, some findings can be drawn:

- (1) The experimental study reveals that the failure morphologies of the axially compressed CFDEST stub columns majorly contain the outward local bulges of the outside EST, the inward bulges of the inside EST and the crushing of the core concrete.
- (2) In light of the experimental study, FE modelling for analysing the axial performance of the CFDEST short column is built and validated by the test outcomes. Then, systematic parametric analyses of their effects on the axial loading mechanical responses of the CFDEST short column are performed.
- (3) The increase in the hollow ratio would lead to successive decreases in the lateral expansion of compressive core concrete and the confinement furnished by the outside steel tube. As a result, both the axial compress capacity and ductility of the CFDEST short column may be gradually weakened within the parameter analytical scope.
- (4) For the axially compressed CFDEST short column, the confining stress provided by the outside EST on core concrete shows obvious heterogeneity, due to the difference in curvature at various points of the cross-section. With an increment in the sectional aspect ratio of the elliptical cross-section, the average confining pressure on concrete is gradually decreased; therefore, its axial load-bearing capacity and ductility coefficient decrease as well.
- (5) This paper proposes a design method for evaluating the axial compress capacity of the CFDEST short column. The calculation formulae are proven to have good accuracy and reliability in prediction.

Author Contributions: Conceptualization, J.L. and Q.S.; methodology, Q.S. and B.L.; software, Q.S. and J.W.; validation, J.L., Q.S. and J.W.; formal analysis, J.L. and Q.S.; investigation, J.L. and Q.S.; resources, Q.S., J.W. and B.L.; data curation, J.L.; writing—original draft preparation, J.L., Q.S. and G.L.; writing—review and editing, Q.S.; visualization, J.L.; supervision, Q.S. and G.L.; project administration, Q.S.; funding acquisition, Q.S. All authors have read and agreed to the published version of the manuscript.

Funding: This research was funded by the “National Natural Science Foundation of China, grant number 52108129”, “Fundamental Research Funds for the Central Universities of China, grant number JZ2021HGQA0249, JZ2021HGTA0156 and PA2021GDSK0081” and “Postdoctoral Research Foundation of China, grant number 2022M713388”.

Data Availability Statement: Data supporting the reported results can be found in public datasets analysed during the study.

Conflicts of Interest: The authors declare no conflict of interest.

References

1. Shams, M.; Saadeghvaziri, M.A. State of the art of concrete-filled steel tubular columns. *ACI Struct. J.* **1997**, *94*, 558–571.
2. Ma, W.C.; Tian, Y.; Zhao, H.L.; Orton, S.L. Time-dependent behavior of reinforced concrete columns subjected to high sustained loads. *J. Struct. Eng.* **2022**, *148*, 04022161. [\[CrossRef\]](#)
3. Wu, L.W.; Tian, Y.; Su, Y.P.; Chen, H.B. Seismic performance of precast composite shear walls reinforced by concrete-filled steel tubes. *Eng. Struct.* **2018**, *162*, 72–83. [\[CrossRef\]](#)
4. Liao, J.; Asteris, P.G.; Cavaleri, L.; Mohammed, A.S.; Lemonis, M.E.; Tsoukalas, M.Z.; Skentou, A.D.; Maraveas, C.; Koopialipour, M.; Armaghani, D.J. Novel fuzzy-based optimization approaches for the prediction of ultimate axial load of circular concrete-filled steel tubes. *Buildings* **2021**, *11*, 629. [\[CrossRef\]](#)
5. Al-Shaar, A.A.; Göğüş, M.T. Flexural behavior of lightweight concrete and self-compacting concrete-filled steel tube beams. *J. Constr. Steel Res.* **2018**, *149*, 153–164. [\[CrossRef\]](#)
6. Zhou, Z.; Zhou, X.H.; Yan, B.; Gan, D. Shear strength of stiffened square thin-walled concrete-filled steel tubular columns. *J. Build. Eng.* **2022**, *58*, 104968. [\[CrossRef\]](#)
7. Le, K.B.; Cao, V.V. Numerical study of circular concrete filled steel tubes subjected to pure torsion. *Buildings* **2021**, *11*, 397. [\[CrossRef\]](#)
8. Ramírez Ortiz, C.; Gutierrez Amador, A.D.; Ramírez Duque, J.L. Numerical analysis of the seismic behavior of a steel beam-to-concrete-filled steel tubular column connection using external diaphragms. *Buildings* **2022**, *12*, 1217. [\[CrossRef\]](#)
9. Stephens, M.T.; Lehman, D.E.; Roeder, C.W. Seismic performance modeling of concrete-filled steel tube bridges: Tools and case study. *Eng. Struct.* **2018**, *165*, 88–105. [\[CrossRef\]](#)
10. Kang, X.; Liu, Y.; Zhao, S. Design calculation for concrete-filled steel tube under soft lateral impact. *Buildings* **2022**, *12*, 1618. [\[CrossRef\]](#)
11. Wang, Z.G.; Wu, H.; Fang, Q.; Wu, J. Experimental study on the residual axial capacity of ultra high performance cementitious composite filled steel tube (UHPCC-FST) column under contact explosion. *Thin-Walled Struct.* **2020**, *147*, 106515. [\[CrossRef\]](#)
12. Moradi, M.J.; Daneshvar, K.; Ghazi-nader, D.; Hajiloo, H. The prediction of fire performance of concrete-filled steel tubes (CFST) using artificial neural network. *Thin-Walled Struct.* **2021**, *161*, 107499. [\[CrossRef\]](#)
13. Alraeeini, A.S.; Nikbakht, E. Corrosion effect on the flexural behaviour of concrete filled steel tubulars with single and double skins using engineered cementitious composite. *Structures* **2022**, *44*, 1680–1694. [\[CrossRef\]](#)
14. *Eurocode 4 1994-1-1:2004; Design of Composite Steel and Concrete Structures-Part 1-1: General Rules and Rules for Buildings.* CEN: Brussels, Belgium, 2004.
15. Han, L.H. *Concrete Filled Steel Tubular Structures—Theory and Practice*, 3rd ed.; Science Press: Beijing, China, 2016. (In Chinese)
16. *AISC 360-05; Specification for Structural Steel Buildings.* AISC: Chicago, IL, USA, 2005.
17. *GB 50396-2014; Technical Code for Concrete Filled Steel Tubular Structures.* Architecture Industrial Press of China: Beijing, China, 2014. (In Chinese)
18. Chang, Z.H.; Azmi, M.R.; Yatim, M.Y.M. Behaviour of Concrete-Filled Double Skin Tubular Short Column with Plate Stiffeners Welded Intermittently under Axial Compression. *Buildings* **2022**, *12*, 567. [\[CrossRef\]](#)
19. Yu, P.; Ren, Z.; Yun, W.; Zhao, Y.; Xu, J. Performance of bolt-welded CFST short columns with different initial imperfections: Experimental and numerical studies. *Buildings* **2022**, *12*, 1352. [\[CrossRef\]](#)
20. Tiwary, A.K. Experimental investigation into mild steel circular concrete-filled double skin steel tube columns. *J. Constr. Steel Res.* **2022**, *198*, 107527. [\[CrossRef\]](#)
21. Hassanein, M.F.; Silvestre, N. New confining stress-based design for rubberised concrete-filled single/double-skin steel tubular short columns. *J. Constr. Steel Res.* **2022**, *197*, 107435. [\[CrossRef\]](#)
22. Li, W.; Wang, T.; Han, L.H. Seismic performance of concrete-filled double-skin steel tubes after exposure to fire: Experiments. *J. Constr. Steel Res.* **2019**, *154*, 209–223. [\[CrossRef\]](#)

23. Hou, C.; Han, L.H.; Zhao, X.L. Behaviour of circular concrete filled double skin tubes subjected to local bearing force. *Thin-Walled Struct.* **2015**, *93*, 36–53. [[CrossRef](#)]
24. Vernardos, S.; Gantes, C. Experimental behavior of concrete-filled double-skin steel tubular (CFDST) stub members under axial compression: A comparative review. *Structures* **2019**, *22*, 383–404. [[CrossRef](#)]
25. Hassanein, M.F.; Kharoob, O.F. Compressive strength of circular concrete-filled double skin tubular short columns. *Thin-Walled Struct.* **2014**, *77*, 165–173. [[CrossRef](#)]
26. Ayough, P.; Ramli Sulong, N.H.; Ibrahim, Z.H. Analysis and review of concrete-filled double skin steel tubes under compression. *Thin-Walled Struct.* **2020**, *148*, 106495. [[CrossRef](#)]
27. Ren, Q.X.; Han, L.H.; Lam, D.; Hou, C. Experiments on special-shaped CFST stub columns under axial compression. *J. Constr. Steel Res.* **2014**, *98*, 123–133. [[CrossRef](#)]
28. Shen, Y.; Tu, Y.; Huang, W. Flexural strength evaluation of multi-cell composite L-shaped concrete-filled steel tubular beams. *Buildings* **2022**, *12*, 39. [[CrossRef](#)]
29. Fang, H.; Chan, T.M.; Young, B. Structural performance of concrete-filled cold-formed high-strength steel octagonal tubular stub columns. *Eng. Struct.* **2021**, *239*, 112360. [[CrossRef](#)]
30. Wang, J.F.; Liu, W.; Shen, Q.H.; Li, J.Z.; Han, Z.H. Experimental investigation and theoretical analysis of axially-loaded concrete-filled elliptical tubes with circumferential gaps. *Thin-Walled Struct.* **2022**, *181*, 110100. [[CrossRef](#)]
31. Cai, Y.C.; Quach, W.M.; Young, B. Experimental and numerical investigation of concrete-filled hot-finished and cold-formed steel elliptical tubular stub columns. *Thin-Walled Struct.* **2019**, *145*, 106437. [[CrossRef](#)]
32. Xing, W.B.; Shen, Q.H.; Wang, J.F.; Sheng, M.Y. Performance and design of oval-ended elliptical CFT columns under combined axial compression-torsion. *J. Constr. Steel Res.* **2020**, *172*, 106148. [[CrossRef](#)]
33. Yang, H.; Lam, D.; Gardner, L. Testing and analysis of concrete-filled elliptical hollow sections. Testing and analysis of concrete-filled elliptical hollow sections. *Eng. Struct.* **2008**, *30*, 3771–3781. [[CrossRef](#)]
34. Yang, H.; Liu, F.Q.; Chan, T.M.; Wang, W. Behaviours of concrete-filled cold-formed elliptical hollow section beam-columns with varying aspect ratios. *Thin-Walled Struct.* **2017**, *120*, 9–28. [[CrossRef](#)]
35. Dai, X.; Lam, D. Numerical modelling of the axial compressive behaviour of short concrete-filled elliptical steel columns. *J. Constr. Steel Res.* **2010**, *66*, 931–942. [[CrossRef](#)]
36. Mahgub, M.; Ashour, A.; Lam, D.; Dai, X. Tests of self-compacting concrete filled elliptical steel tube columns. *Thin-Walled Struct.* **2017**, *110*, 27–34. [[CrossRef](#)]
37. Jamaluddin, N.; Lam, D.; Dai, X.H.; Ye, J. An experimental study on elliptical concrete filled columns under axial compression. *J. Constr. Steel Res.* **2013**, *87*, 6–16. [[CrossRef](#)]
38. Liu, F.Q.; Wang, Y.Y.; Chan, T.M. Behaviour of concrete-filled cold-formed elliptical hollow sections with varying aspect ratios. *Thin-Walled Struct.* **2017**, *110*, 47–61. [[CrossRef](#)]
39. Hassanein, M.F.; Patel, V.I.; Hadidy, A.M.; Abadi, H.A.; Elchalakanid, M. Structural behaviour and design of elliptical high-strength concrete-filled steel tubular short compression members. *Eng. Struct.* **2018**, *173*, 495–511. [[CrossRef](#)]
40. Ren, Q.X.; Han, L.H.; Lam, D.; Li, W. Tests on elliptical concrete filled steel tubular (CFST) beams and columns. *J. Constr. Steel Res.* **2014**, *99*, 149–160. [[CrossRef](#)]
41. Zhang, T.; Gong, Y.Z.; Ding, F.X.; Liu, X.M.; Yu, Z.W. Experimental and numerical investigation on the flexural behavior of concrete-filled elliptical steel tube (CFET). *J. Build. Eng.* **2021**, *41*, 102412. [[CrossRef](#)]
42. Uenaka, K.; Tsunokake, H. Behavior of concrete filled elliptical steel tubular deep beam under bending-shear. *Structures* **2017**, *10*, 89–95. [[CrossRef](#)]
43. Uenaka, K.; Tsunokake, H. Concrete filled elliptical steel tubular members with large diameter-to-thickness ratio subjected to bending. *Structures* **2016**, *5*, 58–66. [[CrossRef](#)]
44. Wang, J.F.; Tao, S.Q.; Shen, Q.H.; Sheng, M.Y. Mechanical performance and bearing capacity calculation of elliptical CFST members subjected to compression, bending and torsion. *Prog. Steel Build. Struct.* **2022**, *24*, 45–55. (In Chinese)
45. Xu, Y.W.; Yao, J.; Hu, F.; Zhou, Y.; Jiang, S. Seismic behavior of elliptical concrete-filled steel tubular columns under combined axial compression and cyclic lateral loading. *Adv. Mater. Sci. Eng.* **2021**, *1*, 5892788. [[CrossRef](#)]
46. Espinos, A.; Romero, M.L.; Serra, E.; Hospitaler, A. Experimental investigation on the fire behaviour of rectangular and elliptical slender concrete-filled tubular columns. *Thin-Walled Struct.* **2015**, *93*, 137–148. [[CrossRef](#)]
47. Espinos, A.; Romero, M.L.; Portolés, J.M.; Hospitaler, A. Ambient and fire behavior of eccentrically loaded elliptical slender concrete-filled tubular columns. *J. Constr. Steel Res.* **2014**, *100*, 97–107. [[CrossRef](#)]
48. Ahmed, M.; Ci, J.C.; Yan, X.F.; Chen, S.C. Nonlinear analysis of elliptical concrete-filled stainless steel tubular short columns under axial compression. *Structures* **2021**, *32*, 1347–1385. [[CrossRef](#)]
49. Sheehan, T.; Dai, X.H.; Chan, T.M.; Lam, D. Structural response of concrete-filled elliptical steel hollow sections under eccentric compression. *Eng. Struct.* **2012**, *45*, 314–323. [[CrossRef](#)]
50. McCann, F.; Gardner, L.; Qiu, W. Experimental study of slender concrete-filled elliptical hollow section beam-columns. *J. Constr. Steel Res.* **2015**, *113*, 185–194. [[CrossRef](#)]
51. Shen, Q.H.; Li, J.Z.; Wang, J.F. Experimental, numerical and design investigations on the performance of axially-loaded ECFT stub columns with spherical-cap gaps. *Structures* **2022**, *46*, 109–127. [[CrossRef](#)]

52. GB/T2975-2018; Steel and Steel Products-Location and Preparation of Samples and Test Pieces for Mechanical Testing. General Administration for National Market Supervision: Beijing, China, 2018. (In Chinese)
53. GB/T 50081-2019; Standard for Test Methods of Concrete Physical and Mechanical Properties. Ministry of Housing and Urban-Rural Construction of the People's Republic of China: Beijing, China, 2019. (In Chinese)
54. Shen, Q.H.; Wang, F.Q.; Wang, J.F.; Ma, X.F. Cyclic behaviour and design of cold-formed round-ended concrete-filled steel tube columns. *J. Constr. Steel Res.* **2022**, *190*, 107089. [[CrossRef](#)]
55. Wang, J.F.; Xiao, Q.; Shen, Q.H.; Sheng, M.Y. Analysis on the axial behavior of CFRP wrapped circular CFST stub columns with initial concrete imperfection. *Prog. Steel Build. Struct.* **2021**, *23*, 44–53. (In Chinese)
56. Huang, H.; Han, L.H.; Tao, Z.; Zhao, X.L. Analytical behaviour of concrete-filled double skin steel tubular (CFDST) stub columns. *J. Constr. Steel Res.* **2010**, *66*, 542–555. [[CrossRef](#)]
57. Han, L.H.; Ren, Q.X.; Li, W. Tests on stub stainless steel–concrete–carbon steel double-skin tubular (DST) columns. *J. Constr. Steel Res.* **2011**, *67*, 437–452. [[CrossRef](#)]
58. Tao, Z.; Han, L.H.; Zhao, X.L. Behaviour of concrete-filled double skin (CHS inner and CHS outer) steel tubular stub columns and beam-columns. *J. Constr. Steel Res.* **2004**, *60*, 1129–1158. [[CrossRef](#)]